JOURNAL OF SYNCHROTRON RADIATION
ISSN 1600-5775

Diffraction apparatus and procedure in tomography X-ray diffraction imaging for biological cells at cryogenic temperature using synchrotron X-ray radiation

Amane Kobayashi,[a,b]‡ Yuki Takayama,[a,b,c]‡ Koji Okajima,[a,b] Mao Oide,[a,b] Takahiro Yamamoto,[a,b] Yuki Sekiguchi,[a,b] Tomotaka Oroguchi,[a,b] Masayoshi Nakasako,[a,b]* Yoshiki Kohmura,[b] Masaki Yamamoto,[b] Takahiko Hoshi[d] and Yasufumi Torizuka[d]

[a]Department of Physics, Faculty of Science and Technology, Keio University, 3-14-1 Hiyoshi, Kohoku-ku, Yokohama, Kanagawa 223-8522, Japan, [b]RIKEN SPring-8 Center, 1-1-1 Kouto, Sayo, Sayo-gun, Hyogo 679-5148, Japan, [c]Graduate School of Material Science, University of Hyogo, 3-2-1 Kouto, Kamigori-cho, Ako-gun, Hyogo 678-1297, Japan, and [d]RIGAKU-Aihara Seiki, 2-24 Higasimatsubara, Hakonegasaki, Mizuho-cho, Nishitama-gun, Tokyo 190-1222, Japan. *Correspondence e-mail: nakasako@phys.keio.ac.jp

Received 24 April 2018
Accepted 7 September 2018

Edited by A. F. Craievich, University of São Paulo, Brazil

‡ These authors contributed equally to this work.

Keywords: X-ray diffraction imaging; tomography; biological cells; cryogenic experiments.

Supporting information: this article has supporting information at journals.iucr.org/s

X-ray diffraction imaging is a technique for visualizing the structure of biological cells. In X-ray diffraction imaging experiments using synchrotron radiation, cryogenic conditions are necessary in order to reduce radiation damage in the biological cells. Frozen-hydrated biological specimens kept at cryogenic temperatures are also free from drying and bubbling, which occurs in wet specimens under vacuum conditions. In a previous study, the diffraction apparatus KOTOBUKI-1 [Nakasako *et al.* (2013), *Rev. Sci. Instrum.* **84**, 093705] was constructed for X-ray diffraction imaging at cryogenic temperatures by utilizing a cryogenic pot, which is a cooling device developed in low-temperature physics. In this study a new cryogenic pot, suitable for tomography experiments, has been developed. The pot can rotate a biological cell over an angular range of $\pm 170^\circ$ against the direction of the incident X-ray beam. Herein, the details and the performance of the pot and miscellaneous devices are reported, along with established experimental procedures including specimen preparation. The apparatus has been used in tomography experiments for visualizing the three-dimensional structure of a *Cyanidioschyzon merolae* cell with an approximate size of 5 µm at a resolution of 136 nm. Based on the experimental results, the necessary improvements for future experiments and the resolution limit achievable under experimental conditions within a maximum tolerable dose are discussed.

1. Introduction

To gain a better understanding of the fundamental processes that occur inside biological cells, various types of imaging techniques have been developed. For instance, fluorescence light microscopy (LM) has been applied to *in situ* observations of the distribution and movements of biological macromolecules labeled by fluorescence dyes or fluorescence proteins in cells (Huang *et al.*, 2009). Super-resolution microscopy made a breakthrough in the visualization of fluorescence probes at a resolution higher than 200 nm (Hell & Wichmann, 1994). Electron microscopy has also contributed to the elucidation of cellular structures (Jaffe *et al.*, 1973; Oikonomou *et al.*, 2016). Due to the strong interactions between free electrons and the electrostatic potential produced by the constituent atoms of specimens, whole cells with thicknesses greater than 1 µm are opaque in transmission

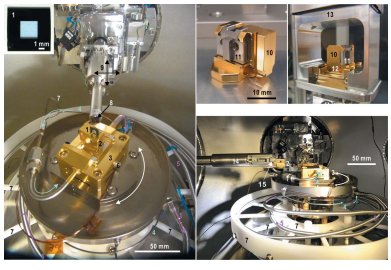

electron microscopy (TEM). Therefore, TEM imaging to visualize structures of cells at a lateral resolution of 10 nm has been applied to 100 nm-thick slices of chemically fixed cells (Robards & Sleytr, 1985), cells embedded in vitreous ice (Al-Amoudi *et al.*, 2004; Hsieh *et al.*, 2006) or alternatively to the thin periphery of cells (Zhao *et al.*, 2014; von Appen & Beck, 2016).

There are two imaging techniques utilizing X-rays. Soft X-ray transmission microscopy has been applied to studies on the structures of biological tissues and cells by using Fresnel zone plates and X-rays with wavelengths in the water window (Kirz *et al.*, 1995; Shapiro *et al.*, 2005). This imaging technique visualizes the absorption contrast of materials comprising biological cells, and a whole cell was reconstructed at an isotropic resolution of 70 nm based on Fourier ring correlation analysis and a local resolution of 36 nm confirmed by the Rayleigh criterion (Schneider *et al.*, 2010).

X-ray diffraction imaging (XDI) is an alternative X-ray imaging technique (Miao *et al.*, 1999, 2015; Nakasako, 2018) and is still under progress in comparison with the sophisticated imaging techniques described above. Since this technique directly visualizes the distribution of electron densities inside biological cells with a natural contrast, the obtainable structural information on cellular structures is substantially different from that of soft X-ray transmission microscopy. X-rays with short wavelengths have a high penetration power into thick objects without multiple scattering, and allow us to investigate the electron density distribution inside thick specimens without the need for sectioning. Indeed, several experiments have successfully demonstrated the potential of XDI for studying the internal structure of whole biological cells and cellular organelles with dimensions in the micrometre range at a spatial resolution of several tens of nanometres (Nishino *et al.*, 2009; Jiang *et al.*, 2010; Song *et al.*, 2014).

In an XDI experiment the diffraction pattern of a single non-crystalline biological cell is collected by an area detector under X-ray illumination with a high transverse coherence. An electron density map of the particle, which is projected along the direction of the incident X-ray beam, is reconstructed from the diffraction pattern alone by using phase-retrieval (PR) algorithms (Fienup, 1982; Rodriguez *et al.*, 2013). However, the three-dimensional (3D) structure of a particle is difficult to speculate from a single projection map, except for the case where the representative structures of the particle appear in the projection maps (Takayama *et al.*, 2015). Therefore, tomography experiments are necessary to visualize the 3D structure of the specimen particle.

In tomography XDI experiments a series of diffraction patterns are collected by rotating the specimen around an axis perpendicular to the direction of the incident X-ray beam (Fig. 1*a*). There are two types of algorithms for 3D reconstruction. One is the back-projection method applied to a set of projection electron density maps, which are retrieved from the diffraction patterns of a specimen particle at different orientations with respect to the direction of the incident X-rays (Kodama & Nakasako, 2011; Oroguchi & Nakasako, 2013) (Fig. 1*b*). The other is the 3D PR method applied to the

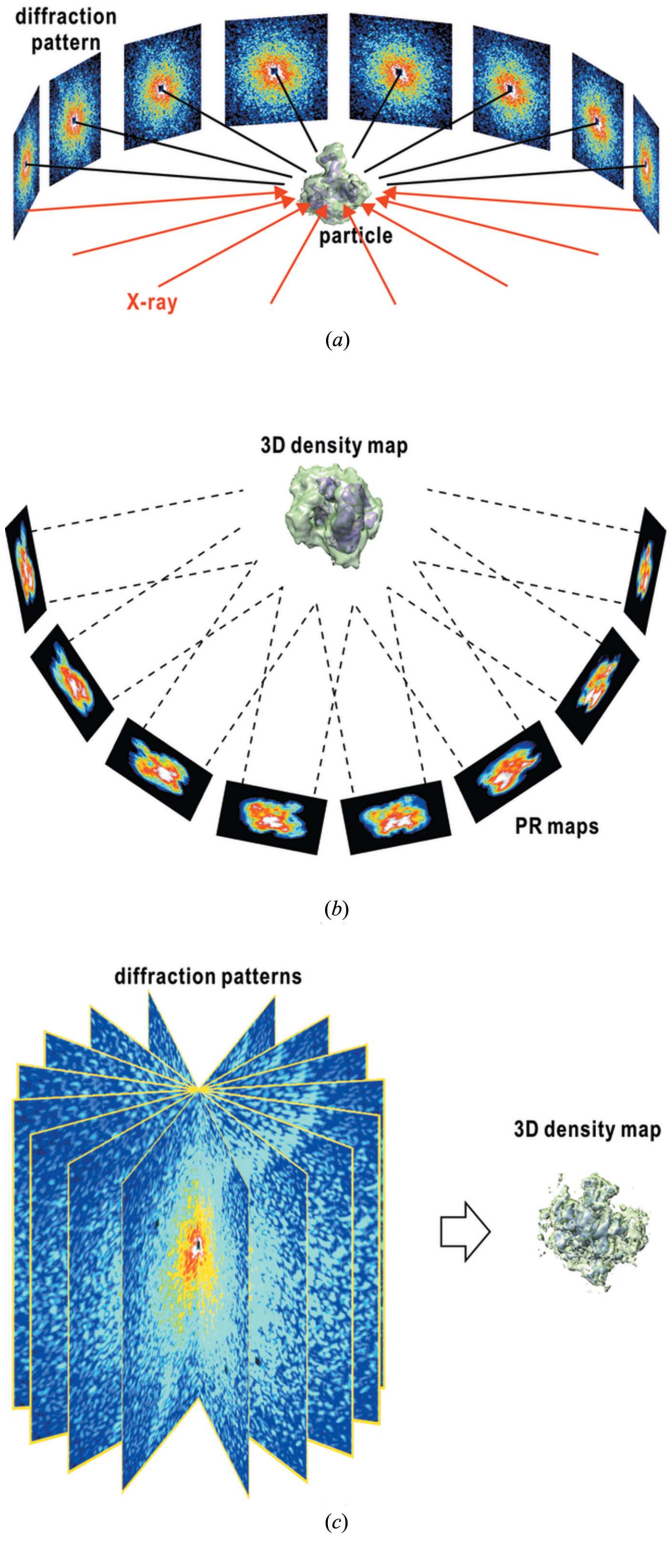

Figure 1
(*a*) Schematic illustration of a tomography XDI experiment. To collect the 3D distribution of diffraction intensity of a specimen particle the specimen is rotated against the direction of the incident X-ray beam. (*b*) Schematic illustration of 3D reconstruction by using the back-projection method applied to PR projection maps, each of which is retrieved from a diffraction pattern. (*c*) Reconstruction of a 3D map by using the 3D PR method applied to the 3D distribution of diffraction intensity reconstructed from the diffraction patterns.

3D distribution of diffraction intensity that satisfies the oversampling condition up to a desired resolution (Nishino *et al.*, 2009; Jiang *et al.*, 2010; Song *et al.*, 2014) (Fig. 1*c*). Tomography XDI was successfully applied to reveal whole structures of thick specimens such as synthesized particles (Miao *et al.*, 2002) and dried or chemically fixed biological cells (Nishino *et al.*, 2009; Jiang *et al.*, 2010) that are typically opaque to TEM at a resolution higher than LM.

Tomography XDI experiments of biological cells and organelles with small scattering cross sections were performed in a vacuum to reduce scattering from and absorption by air. However, a vacuum environment is hazardous to biological specimens because a fully hydrated state is required to maintain their functional structures. Therefore, to avoid the degradation of specimens due to the boiling of water and adiabatic expansion under vacuum conditions, most XDI experiments are performed on dried and chemically fixed biological specimens (Nishino *et al.*, 2009; Jiang *et al.*, 2010). Thus, we are hesitant to accept the experimental results for these specimens. Even under a high humidity environment at ambient temperature (Song *et al.*, 2014) it is difficult to deny the possibility that a chemically fixed biological specimen may be subject to radiation damage, as reported in a study on macromolecular crystals under X-ray irradiation (Boutet & Robinson, 2006).

One of the methods for reducing radiation damage of biological specimens was innovated in TEM to study the structures of biological specimens in their frozen-hydrated state (Dubochet & McDowall, 1981; Dubochet *et al.*, 1982). The mechanism to reduce radiation damage of biological specimens is discussed in cryogenic TEM (Baker & Rubinstein, 2010; Adrian *et al.*, 1984) and cryogenic X-ray protein crystallography (Meents *et al.*, 2010). Frozen-hydrated specimens maintained at cryogenic temperatures are suitable for reducing radiation damage in a long-term exposure necessary in tomography XDI experiments, as demonstrated by the pioneering work on a bacterial cell by Rodriguez *et al.* (2015). Specimens that are frozen-hydrated by the flash-cooling method are almost free from dehydration and retain their functional structures. In fact, biological cells returned from cryogenic temperatures to ambient temperature have been found to be still alive (Gibson & Khoury, 1986).

In a previous study we developed the diffraction apparatus KOTOBUKI-1 for XDI experiments at cryogenic temperatures (Nakasako *et al.*, 2013; Oroguchi *et al.*, 2015). The apparatus was equipped with a cryogenic pot mounted on a rotation stage inside its vacuum chamber. The cryogenic pot is a key device in cryogenics and low-temperature physics using an evaporation refrigerator (DeLong *et al.*, 1971). However, the rotation of a specimen was limited to within $\pm 60^\circ$ against the direction of the incident X-ray beam due to a geometrical hindrance of the pot, which stopped the incident X-ray beam at higher rotation angles. In this study we have developed a new cryogenic pot that enables us to rotate specimen particles over an angular range of $\pm 170^\circ$.

In addition, by incorporating the specimen preparation techniques in cryo-TEM (Robards & Sleytr, 1985; Grassucci *et al.*, 2007) and X-ray microscopy (Maser *et al.*, 2000), we also developed procedures for preparing frozen-hydrated biological cells at desired cell cycles without chemical modification. By using the new version of the diffraction apparatus we performed cryogenic tomography XDI experiments to reconstruct the 3D electron density map of a biological cell with an approximate size of 5 µm. Here we report details of the new cryogenic pot, specimen preparation including its weak points, and its application to structure analysis.

2. Description of the devices

2.1. Cryogenic pot

The new cryogenic pot dedicated to tomography XDI experiments was designed to rotate the specimens over an angular range of $\pm 170^\circ$ with respect to the direction of the incident X-ray beam. The pot is a gold-coated block of oxygen-free copper with a flat-top shape (Fig. 2*a*). It has a reservoir with an approximate volume of 8 mL for storing liquid nitrogen. Liquid nitrogen is supplied to the reservoir from a liquid-nitrogen dewar mounted on the vacuum chamber of the diffraction apparatus through a high-impedance capillary of an annealed cupronickel tube. The reservoir is also connected to a scroll pump outside the chamber through a flexible exhaust pipe. The flow rate of the liquid nitrogen was controlled using a needle valve at the outlet port of the dewar and another connected to the scroll pump.

The pot is connected to a goniometer by a set of polymer rods (TORLON-TR4203 polymer; Solvay Advanced Polymers), which have a low thermal conductivity and work as vibration isolators. Both the capillary and the exhaust pipe were arranged circularly around the pot for smooth rotation of the pot (Fig. 2*a*). In the goniometer a translation stage for the vertical direction (ZA07A-R3S-1Y; Kohzu Precision, Japan) and two translation stages for the horizontal plane (MVXA07A-R1-1B; Kohzu Precision, Japan) are mounted on a rotation stage (MVRA10A-W; Kohzu Precision, Japan). Each of the three translation stages provides a maximum stroke of 3 mm with a resolution of 25 nm. The positional reproducibility of each stage was approximately 0.2 µm, because of the backlash of gears, precision of ball guides and hysteresis effects on the stages. The nominal positional fluctuation of the specimen on the pot filled with liquid nitrogen is smaller than 0.4 µm. The angular resolution of the rotation stage is 0.004°. The sphere of confusion of the rotation stage at the specimen position was approximately 10 µm/360°. Therefore, positional adjustment of a specimen against the position of the incident X-ray beam is necessary after every rotation of the rotation stage in tomography experiments.

The motorized devices in the KOTOBUKI-1 diffraction apparatus were controlled through a GPIB interface using the *IDATEN* program suite (Sekiguchi *et al.*, 2014*a*) coded using the LabVIEW language (National Instruments, USA). Another program suite was developed for tomography XDI experiments using the LabVIEW language. The program semi-automatically executes a series of sequential actions in

diffraction data collection. After we put the rotation range and step into the program, the program semi-automatically controls the rotation, the scan of the specimen against the X-ray beam position, the collection of diffraction patterns from the specimen and silicon nitride membrane alone as the background, and the transfer of recorded patterns from the detector system to PC for data storage and analyses.

2.2. Specimen holder

We use a silicon frame of size 7.5 mm × 7.5 mm and thickness 0.2 mm (Silson, UK) as a specimen disk. Each frame has a 3 mm × 3 mm window of silicon nitride (Si_3N_4) (hereafter SiN) membrane with a thickness of 100 nm (upper-left inset in Fig. 2*a*). Since the deviation of the thickness is within 1 nm, the membrane is almost uniform. In addition, the roughness of the membrane surface was very small, with its root mean squared being within the range 0.5–1.0 nm (Silson, UK).

To deliver a flash-cooled specimen disk from a liquid-nitrogen bath to the cryogenic pot inside the vacuum chamber of the diffraction apparatus, we designed and developed a specimen holder that is composed of a main body made of gold-coated oxygen-free copper and a stainless plate (Fig. 2*b*). Each specimen disk is sandwiched between the main body and the plate. A small neodymium magnet buried in the main body attracts the plate to assist the thermal contact between the holder and disk. The cooled holder with a specimen disk is brought to a load-lock chamber of the apparatus by using a specially designed carrier (Fig. 2*c*). Immediately after placing the carrier inside the load-lock chamber, the chamber is evacuated. Then the specimen holder is brought to the cryogenic pot by a transfer rod with claws and fork to catch the holder during the delivery (Fig. 2*d*).

Prior to the diffraction experiments, we measured the temperature of the specimen disk mounted on the cryogenic pot. In the measurement, after a thermocouple was attached to the disk mounted on the pot, liquid nitrogen was supplied to the pot. Thermal contact between the holder and the pot ensured that the temperature of the specimen disk was maintained within the temperature range 85–95 K. At this temperature, sublimation of water molecules from frozen-hydrated biological cells is known to be suppressed (Dubochet *et al.*, 1988).

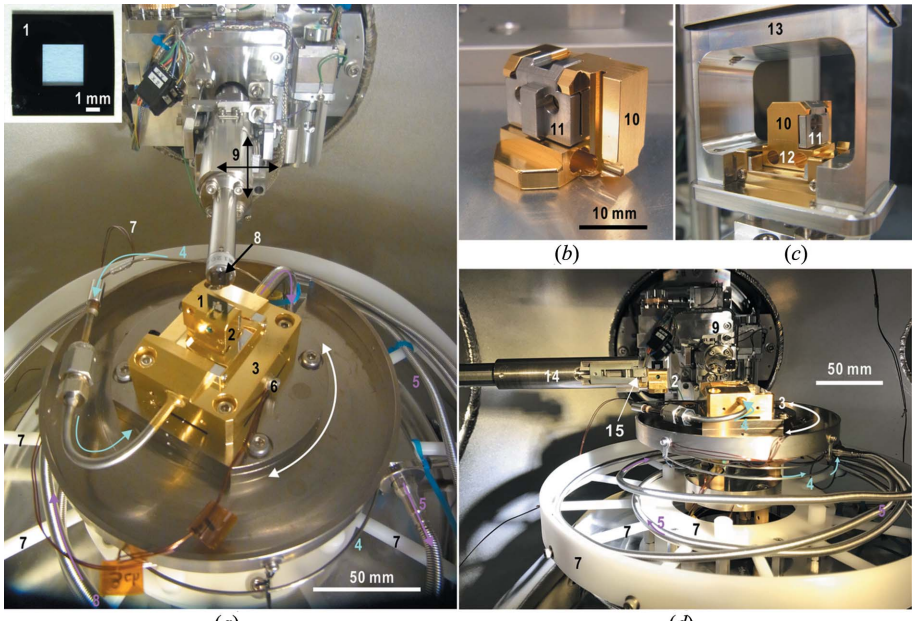

Figure 2
(*a*) Top view of the cryogenic pot in the vacuum chamber of the KOTOBUKI-1 diffraction apparatus. A specimen disk (1) carrying a single biological cell is fixed to a specimen holder (2). The holder is mounted on the cryogenic pot (3), which is connected to a goniometer. Liquid nitrogen is supplied to the pot through a high-impedance cupronickel capillary (4). The cyan-colored arrows indicate the flow direction of liquid nitrogen in the capillary with an inner diameter of 0.75 mm. The magenta-colored arrows show the direction of nitrogen gas flow in the flexible exhaust pipe (5) from the pot to the scroll pump. The temperatures of the pot, the capillary and the pipe are monitored by thermocouples (6). The capillary (4) and exhaust pipe (5) are circularly arranged on a frame made of polychlorotrifluoroethylene (7). The X-ray beam arrives at the specimen position through a silicon frame (8) fixed to a motorized device (9) for positioning. (*b*) Specimen holder composed of a main body (10) and a plate to fix the specimen disk (11). A pair of holes (12) for accepting a fork at the tip of a transfer rod is machined in the lower part of the main body. (*c*) A hanger frame (13) of a carrier for the delivery of the specimen holder from a liquid-nitrogen bath to the load-lock chamber of the diffraction apparatus. (*d*) Snapshot of the transfer rod (14) bringing the specimen holder from the load-lock chamber to the cryogenic pot. The transfer rod has a pair of claws and fork at the tip (15).

3. Experimental procedures and structural analyses

3.1. Specimen preparation

SiN membranes of specimen disks are hydrophobic and have low electron conductivity. Both sides of each SiN membrane were coated with carbon layers using a JEE-420 vacuum evaporator (JEOL, Japan) (Fig. 3*a*). The thickness of the layer was approximately 15 nm. The layers are necessary for the subsequent poly L-lysine (PLL) coating and also for the diffusion of electrons produced by X-ray exposure. Each carbon-coated SiN membrane was treated with a 0.1 mg mL^{-1} solution of PLL with a molecular weight of approximately 300000 (Sigma-Aldrich, USA) for the adhesion of biological cells to the membrane (Fig. 3*a*) (Kobayashi *et al.*, 2016*a*). After a 30 min treatment, unbound PLL was washed out by distilled water.

Biological cells were harvested at desired phases of the cell cycle. Specimen preparation for tomography XDI experiments was carried out by using a specimen preparation system, which comprised a HUM-1 moist-air generator (Rigaku, Japan), a custom-made sample preparation chamber fixed on the specimen stage of an IX71

optical microscope (Olympus, Japan), and a Celltram Vario micro-injector connected to an InjectMan NI2 motor-controlled micro-manipulator (Eppendorf, USA) (Takayama & Nakasako, 2012). The system allowed the preparation of specimens to maintain their hydrated and functional states under a maximum relative humidity of 94%. The maximum achievable temperature of the chamber is approximately 300 K, while cells are often incubated at approximately 310 K. To avoid degradation of the cells by the sudden decrease of temperature in the chamber, cells are incubated at 300 K for two days prior to specimen preparation.

A single cell was placed at about the center of the membrane using a capillary tube of 15 µm inner diameter [TransferTip (ES), Eppendorf, USA] connected to the micro-injector (Takayama & Nakasako, 2012) (Fig. 3*a*). The membrane was centered in the field of view of the microscope by referring to the edges of the silicon frame. This procedure was monitored using the IX71 light microscope with a magnification range from 600 or 900. In this magnification range, single biological cells of size 5 µm can be distinguished from their aggregates (Takayama & Nakasako, 2012).

When a single cell was adsorbed onto the PLL layer formed on the SiN membrane, the Brownian motion of the cell was significantly reduced. In our experience it took within 1 min after the cell approached the PLL layer. Then, an excess amount of the buffer solution around the cell was removed by the tip of the capillary. It should be noted that removal of too much buffer solution may induce excessive adhesion of a cell to the membrane due to the surface tension of the remaining buffer and the subsequent structural deformation (see the *Results* section).

We used a liquid ethane device for flash-cooling specimen disks (Fig. 3*b*) (Takayama & Nakasako, 2012; Kobayashi *et al.*, 2016*a*). Liquid ethane was produced in an aluminium cap cooled by liquid nitrogen in a box made of polystyrene. After acquiring an LM image to record the position of a specimen particle relative to the edges of the silicon frame (Fig. 3*c*), the specimen disk was immersed at a speed of 1 m s^{-1} into the liquid ethane, which was maintained at approximately 85 K. The cooled specimen was lifted up from the liquid ethane and was kept in an atmosphere of cold nitrogen gas at around 120 K. Then, we investigated whether or not the specimen particle remained on the SiN membrane by using a telescope with a long working distance (UWZ-200; Union Optics, Japan) (Fig. 3*b*). Simultaneously, liquid ethane remaining on the surface of the specimen disk was evaporated in 5 min. After the examination (Fig. 3*c*), the specimen disk was kept in a storage box in liquid nitrogen until its use in the tomography XDI experiments.

Micro-hexagonal ice, cubic ice and/or solid ethane gave intense streak patterns in the small-angle region due to diffraction and/or reflection of X-rays by them (Kobayashi *et al.*, 2016*a*). However, we observed few streak patterns during scans on specimen disks in the XDI experiment. Therefore, we concluded that the specimens prepared by the procedure described above were free from contamination of ice and solid ethane.

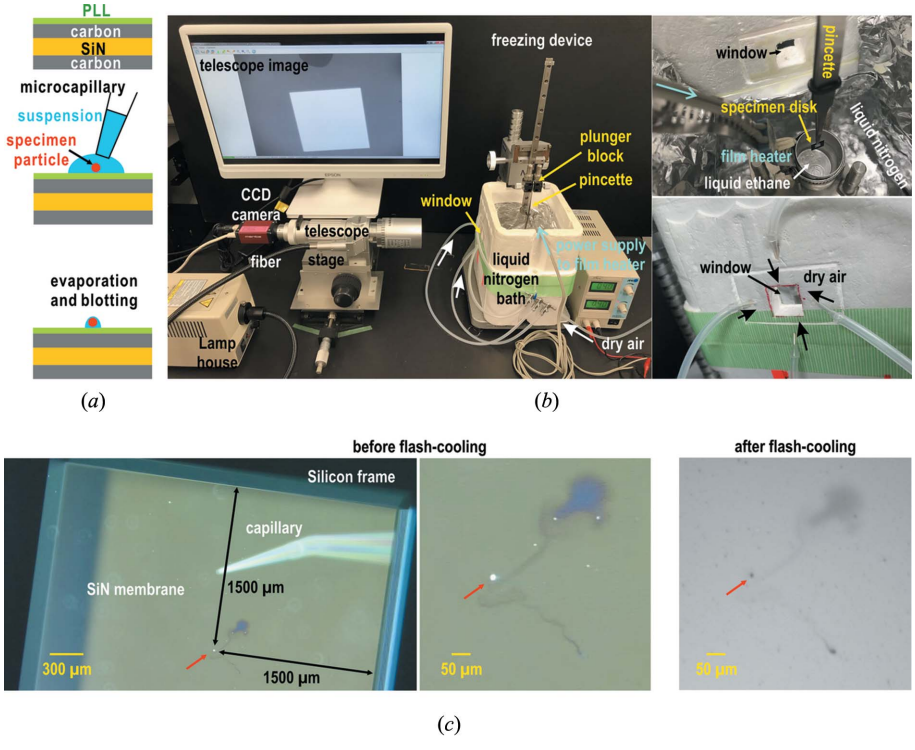

Figure 3
(*a*) Schematic illustration showing the procedure to set a specimen particle on a PLL-coated silicon nitride membrane. (*b*) Photograph of the flash-cooling device with a telescope for checking flash-cooled specimens. A specimen disk is plunged into liquid ethane kept at 85 K by using a film heater to prevent solidification. A telescope with a long working distance was placed outside the liquid-nitrogen bath to monitor the flash-cooled specimen particle through a slide glass fixed to a window of the liquid-nitrogen bath. The upper right panel shows an arrangement of devices inside the liquid-nitrogen bath. Dry air is supplied to the surface of the slide glasses to prevent dew formation (lower right panel). (*c*) LM image of a specimen on a silicon nitride membrane (left panel) and a magnified image (middle) before flash-cooling. The right-hand panel shows a telescope view of the specimen after flash-cooling. The specimen particle is indicated by a red arrow in each panel. In this case, the remained buffer near the specimen particle (a cloud-like object at the upper right) is a good landmark to identify the position of the particle in all images.

3.2. Experimental setup

Tomography XDI experiments were performed in the second experimental hutch of BL29XUL at SPring-8 (Tamasaku *et al.*, 2001) (Fig. 4*a*). We selected X-rays with a wavelength of 0.2254 nm (corresponding to an X-ray photon energy of 5.500 keV) by using a double-crystal monochromator with a fixed-exit geometry. The X-ray wavelength was selected by considering a trade-off among the scattering cross sections of

biological cells, the X-ray diffraction intensity proportional to the second power of the X-ray wavelength, the quantum efficiency of the detector and the absorption of X-rays by biological cells. Higher-order harmonics of the X-rays coming from the monochromator are significantly reduced using a pair of flat platinum mirrors in a fixed-exit geometry set at a glancing angle of 5.5 mrad.

A pinhole with a diameter of 38 μm was placed 1950 mm upstream of the specimen position so that a specimen particle was illuminated by X-ray beams with a high transverse coherence (Fig. 4*b*). The vertical and horizontal profiles of the X-rays diffracted by the pinhole were measured by the knife-edge scan method at the specimen position. Two silicon frames with windows of 100 μm × 100 μm and 120 μm × 120 μm were placed at approximately 420 mm and 15 mm upstream of the specimen position, respectively (Fig. 4*b*). The beveled edges of the windows were used as guard corners to minimize parasitic and background scattering from the upstream optics. The intensity of the incident X-ray beam was kept almost constant by fine-tuning the angle of the first crystal against the second crystal in the monochromator each day.

The intensity of the X-ray beam was monitored by three PIN photodiodes (S3590-09; Hamamatsu Photonics KK, Japan) placed 1 m upstream and 0.1 m downstream of the specimen position, and 0.1 m downstream of the beamstop (Fig. 4*b*). These PIN-photodiodes were placed in the X-ray path only for the intensity measurements. The intensity was counted with a VME counter board (Advme1806; Advanet Inc., Japan) after the signal current of the PIN photodiode was amplified and converted to a pulse train with a current amplifier (Model 428; Keithley, USA) and a V/F converter (DS-VFC2; SEIKO EG and G, Japan). We checked the linearity of the response of the diodes and calibrated a conversion parameter from the count to the number of X-ray photons. By using the intensity, the irradiation dose of a specimen was calculated by recording the intensity profile and the net area of the incident beam irradiating the specimen [see equation (2)].

Diffraction patterns were recorded using an EIGER pixel array detector (DECTRIS, Switzerland) placed 5.8 m downstream of the specimen position. The pixel size of the detector was 75 μm × 75 μm. For X-rays with a photon energy of 5.5 keV used in the experiments, the detector has a dynamic range of up to approximately 4.8×10^5 X-ray photons s^{-1} $pixel^{-1}$ with a linearity in the photon counting. A beamstop of size 1 mm × 1 mm was placed in front of the detector (Fig. 4*b*). The combined use of the pinhole, the silicon frames and the beamstop enabled us to record small-angle diffraction patterns at a resolution of 0.22 μm^{-1} (corresponding to 4.4 μm in real space). For a specimen with a size of approximately 5 μm, speckle patterns in the very small-angle region are necessary for efficient PR calculations (Miao *et al.*, 2005*a*).

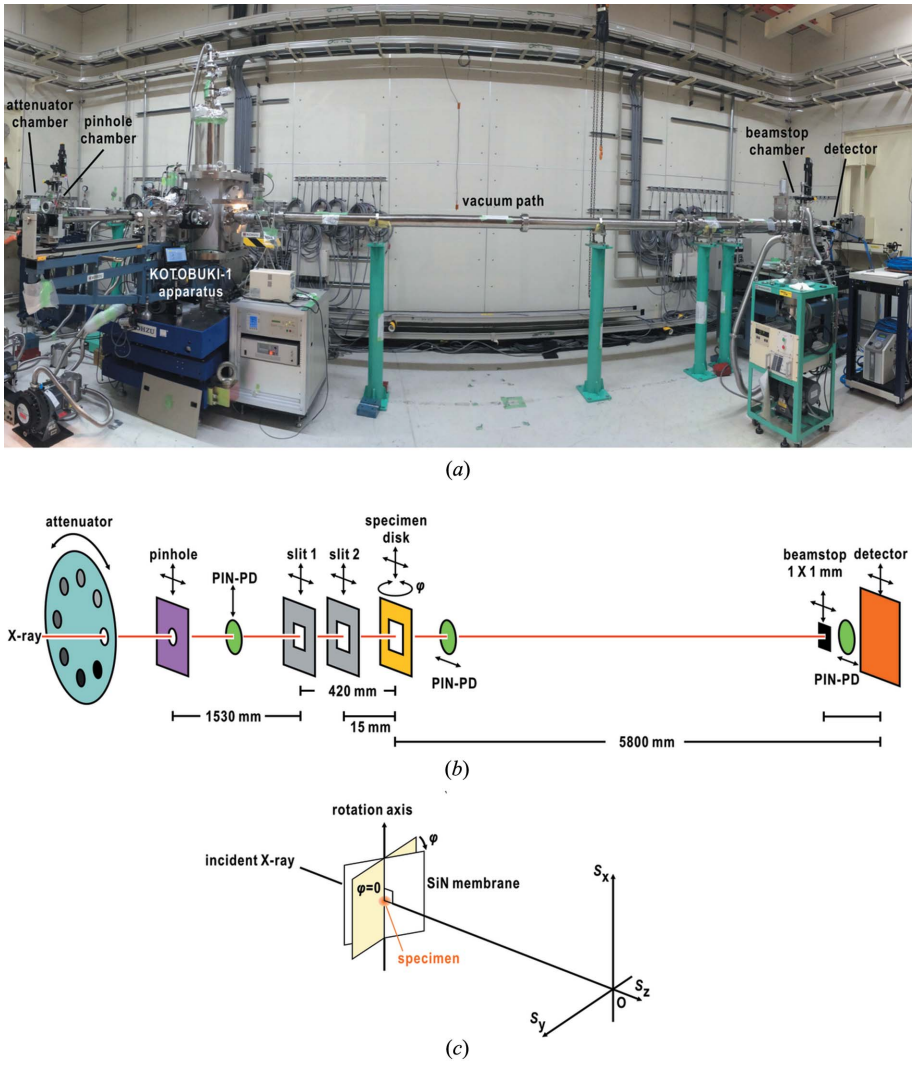

Figure 4
(*a*) View of the experimental setup of the KOTOBUKI-1 diffraction apparatus in the second experimental hutch of BL29XUL at SPring-8. (*b*) Schematic illustration of the arrangement of an attenuator, a pinhole, a set of slits, three PIN-photodiodes (PIN-PD), a beamstop and a detector along the direction of the X-ray beam. (*c*) Definition on the rotation angle of the goniometer and vectors of the reciprocal space used in this study. The goniometer angle φ is measured from the plane normal to the direction of the incident X-ray beam in a clockwise manner.

3.3. Diffraction data collection

In XDI experiments we require an incident X-ray beam with almost perfect spatial coherence, because speckle patterns with a visibility of 1 are necessary for the PR calculations. Prior to XDI tomography experiments, we measured the beam profile along the

vertical and horizontal directions by the knife-edge scan method using a gold wire with a diameter of 300 μm and the PIN photodiode near the specimen position. The profiles gave the beam size at the specimen position (see the *Results* section). Then, we examined the degree of spatial coherence of the incident X-ray beam by comparison with a theoretical prediction, and also from the visibility of the diffraction pattern of a cuboid-shaped cuprous oxide particle (see the *Results* section).

After confirming the spatial coherence of the incident X-ray beam, a specimen disk fixed to a specimen holder was delivered to the cryogenic pot. Then, the specimen holder carrying the specimen disk was set on the holder so that the face of the SiN membrane, on which a specimen particle was adsorbed, looked towards the detector. By scanning the specimen disk against the incident X-ray beam, we first determined the edge positions of the silicon frames relative to the incident X-ray beam. By referring to the LM image acquired before flash cooling (Fig. 3*c*), the specimen disk was moved so that the biological cell was located in the incident X-ray beam. After the specimen disk was scanned in steps of 1 μm with an exposure time of 1 s, the biological cell at 0° rotation angle was set at the position where the sum of the diffraction intensity was the maximum among the scanned points.

Owing to the sphere of confusion of the rotation stage (see §2.1), the position of the biological cell at each rotation angle was adjusted to be located at the center of the incident X-ray beam by scanning the specimen disk against the beam position. The scan range was 5 μm along each of the vertical and horizontal directions. A diffraction pattern was recorded at each scan point by 1 s exposure.

For the structural analysis, a diffraction pattern was recorded at each angle with a 60 s exposure. After the exposure, a background diffraction pattern was recorded for a membrane area more than 50 μm apart from the specimen particle for the same exposure time. Because of the uniformity and roughness of each SiN membrane (see §2.1), the background diffraction patterns collected from the membrane region were almost the same at any place of the membrane.

In 3D reconstruction the achievable maximum resolution is roughly estimated as

$$\text{Maximum resolution} = \pi D/N, \tag{1}$$

where N is the number of projection images of particles in different orientations with respect to the incident beam, and D is the approximate size of the particle (Frank, 2006). This relation determines the minimum number of diffraction patterns, *i.e.* the angular step during rotation of the specimen. In this study a series of diffraction patterns were acquired from a specimen cell with an approximate size of 5 μm and collected at an angular interval of 1.5°. This angular interval was sufficient for reconstruction of a 3D map of the cell at a resolution of 136 nm (see the *Results* section).

The irradiation dose was estimated using the following equation (Jiang *et al.*, 2010),

$$\text{Dose} = \left(\frac{\eta P_{\rm T}}{A}\right)\left(\frac{\mu}{\rho}\right)E_0, \tag{2}$$

where the total number of X-ray photons $P_{\rm T}$ is calculated by multiplying the photon flux density by the total exposure time, and η is the fraction of the intensity irradiating the specimen particle. For a cell of size 5 μm, the fraction was 20.5% of the total diffraction intensity from a pinhole with a diameter of 38 μm. A is the cross section of the specimen (approximately 5 μm × 5 μm) and μ/ρ is the mass absorption coefficient of the biological cells (1.8 $\rm m^2\ kg^{-1}$) (Jiang *et al.*, 2010). E_0 is the energy of the incident X-ray photons (5.5 keV).

3.4. Data processing

At first we masked several hot spots in the detector panels. It was easy to find the hot spots because they displayed very high values of 4.3×10^9 counts $\rm s^{-1}$ $\rm pixel^{-1}$, which was much larger than the diffraction intensity (4×10^5 counts $\rm s^{-1}$ $\rm pixel^{-1}$) from a biological cell of size 5 μm.

The net diffraction pattern was obtained by subtracting the diffraction pattern of a SiN membrane area. The gap regions between the detector panels were filled by a pattern in the region related to Friedel's centrosymmetry, because the biological cells display little anomalous effects at the X-ray wavelength used. Each diffraction pattern was characterized with respect to the degree of centrosymmetry and the maximum resolution. The degree of centrosymmetry is quantitatively evaluated by $C_{\rm sym}$ defined as (Sekiguchi *et al.*, 2014*b*)

$$\begin{aligned} C_{\rm sym} &= \frac{E^2 - O^2}{E^2 + O^2}, \\ E &= \frac{1}{2}\sum_{x,y}\left[I(\mathbf{S}) + I(-\mathbf{S})\right], \\ O &= \frac{1}{2}\sum_{x,y}\left[I(\mathbf{S}) - I(-\mathbf{S})\right], \end{aligned} \tag{3}$$

where $I(\mathbf{S})$ is the intensity in a targeted region of interest (ROI) and $I(-\mathbf{S})$ is the intensity in its symmetry mate with respect to the pixel assumed as the center of the diffraction pattern. In this study, ROIs for the calculation of $C_{\rm sym}$ were set in the resolution range from 7.4 to 15.5 $\rm \mu m^{-1}$. The maximum resolution of a diffraction pattern is defined as the highest resolution shell, where the signal-to-noise ratios of the speckle peaks are greater than 3.

3.5. Phase retrieval calculation for projection electron density maps

For a particle with a diameter of approximately 5 μm, the Ewald sphere can be approximated as a plane intersecting the origin in reciprocal space up to a resolution of 29.9 $\rm \mu m^{-1}$ (Oroguchi & Nakasako, 2013). Therefore, the structure factor in the recorded small-angle region can be assumed as the Fourier transform of the electron density map projected along the direction of the incident X-ray beam.

The PR calculations sometimes fail because diffraction patterns miss the data in the small-angle regions due to the beamstop and are modified by Poisson noise in X-ray detection. A pair of PR maps, which reflect the correct shapes of a biological cell, was selected among a number of independent PR calculations of each diffraction pattern by the following procedures. Hereafter, we designate these PR maps as the most probable maps.

At the first stage, 700 independent PR calculations were performed for a diffraction pattern by using the hybrid input–output (HIO) algorithm (Fienup, 1982) and the shrink-wrap (SW) algorithm (Marchesini *et al.*, 2003) at a resolution of 7.34 μm^{-1} (corresponding to 136 nm in real space). Then, the most probable support shape was selected from the 700 maps by multivariate analysis (Sekiguchi *et al.*, 2016). Next, we performed 1000 independent PR calculations under the constraint of the support shape by using the oversampling smoothness algorithm (Rodriguez *et al.*, 2013). To find the most probable pair of PR maps, we used the score defined as

$$T_{ij} = \frac{\sum_{x,y} \left|\rho_i(x,y) - \rho_j(x,y)\right|}{\sum_{x,y} \left|\rho_i(x,y) + \rho_j(x,y)\right|}, \quad (4)$$

where $\rho_i(x, y)$ is the electron density at a pixel position (x, y) of the ith map. As previously reported (Sekiguchi *et al.*, 2017), this score is a good measure for automatically finding the most probable maps from a large number of independently retrieved maps. The most probable map was obtained by averaging a pair of PR maps displaying the smallest T_{ij} of less than 0.2.

A set of the structure amplitudes calculated from the most probable map was compared with that of the experimental observation by the crystallographic R-factor defined as

$$R_F = \frac{\sum_{\mathbf{S}} \left|\left|F_{obs}(\mathbf{S})\right| - K\left|F_{calc}(\mathbf{S})\right|\right|}{\sum_{\mathbf{S}} \left|F_{obs}(\mathbf{S})\right|}, \quad (5)$$

where $|F_{obs}(\mathbf{S})|$ and $|F_{calc}(\mathbf{S})|$ are the experimentally observed structure amplitudes and those calculated from the most probable map, respectively, and K is a scale factor.

3.6. Reconstruction of the 3D electron density map

The 3D electron density map of a specimen was reconstructed using two methods. One method was the use of the weighted back-projection method applied to a set of projection electron density maps (Radermacher, 1988; Herman, 2009). Prior to the 3D reconstruction, PR maps were regularized with respect to the total density, the handedness and the π-rotation by referring to a reference map. In addition, the maps were normalized so that the sum of the electron density was equal among the PR maps. The 3D reconstruction by using the back-projection method was performed using the *TomoJ* plugin implemented in the *ImageJ* program suite (Messaoudii *et al.*, 2007).

The other 3D reconstruction method was the use of 3D PR calculations using the HIO-SW algorithm applied to a 3D diffraction intensity distribution merged from all diffraction patterns according to the previously reported procedure (Kodama & Nakasako, 2011; Oroguchi & Nakasako, 2013). The threshold values for electron density maps used in the SW calculation were varied so that the size of a PR map converged to that of the specimen cell.

4. Results

In this section we first describe the performance of the cryogenic pot and the properties of the X-ray beam diffracted by the pinhole. Next, the results of the tomography XDI experiment and structural analysis are presented for a *Cyanidioschyzon merolae* (*C. merolae*) cell. We also report the weak point of the current specimen preparation using thin membranes by displaying the 3D structure analysis of a *Saccharomyces cerevisiae* (*S. cereviciae*) cell. Finally, the achievable resolution under a maximum tolerable irradiation dose was estimated based on diffraction data collection from the *C. merolae* cell.

4.1. Performance of the cryogenic pot

Two hours after starting the evacuation of the reservoir of the pot and supplying liquid nitrogen, the temperature reached 76 K due to the evaporation cooling effect of the liquid nitrogen in the reservoir (Fig. 5*a*). The temperature of the pot was maintained for more than one week by supplying liquid nitrogen to the dewar following the consumption of approximately 0.5 L h^{-1}. The fluctuation of the temperature was less than 5 K over one week, and the temperature of the biological cells on the specimen disk was maintained at 85–95 K according to the preliminary experiment (see §2.2). The small fluctuation in the temperature during the tomography experiment indicated that the rotation of the pot had little influence on the temperature of the pot. In addition, we experienced no mechanical problems with rotating the pot.

The collection of diffraction patterns necessary for the 3D reconstruction of a biological cell under the condition shown in Table 1 took approximately two days. The total exposure time for recording diffraction patterns from the cell and the membrane (background) and the positional adjustment was 17255 s (Table 1). Most of the time was spent on our careful and manual operation of the control programs, and checking and adjusting the positions of the X-ray beam and the beamstop. Ways of reducing the experiment time will be discussed later.

4.2. Characteristics of X-rays diffracted by a pinhole

The Fresnel–Kirchhoff diffraction formulae (Born & Wolf, 1999) can predict both the intensity profile and phase values of an X-ray wave diffracted from the pinhole with a diameter of 38 μm placed 1950 mm upstream of the specimen position (Fig. 4*b*). The phase values from the theoretical simulation indicated that the diffracted X-ray waves had a good spatial coherence (approximated as a plane wave) within a radius of 5 μm from the center of the peak. The correlation between the

intensity profiles and phase values allowed us to estimate the variation of the phase in the diffracted wave by comparing the experimental and theoretical intensity profiles.

The profile in the vertical direction displayed a full width at half-maximum (FWHM) value of 15 μm, and slightly wider than the theoretical prediction (Figs. 5*b* and 5*c*). However, the profile had an enhancement at 15 μm from the center as predicted. The profile in the horizontal direction displaying a FWHM of 27 μm was approximately 1.5 times larger than the prediction (Fig. 5*d*). This difference would be predominantly attributed to the apparent horizontal divergences of electron bunches passing through the magnetic field of the undulator of the beamline. The comparison between the theoretical and measured profiles indicated that X-rays within a radius of 5 μm from the central peak were of a high transverse coherence, sufficient to perform XDI analysis.

We recorded the diffraction pattern of a cuboid-shaped cuprous oxide particle (Kuo *et al.*, 2007; Oroguchi *et al.*, 2018) with a size of 580 nm, which was placed in the beam center with a high transverse coherence (Fig. 5*e*). Along the cross-shaped flare, the diffraction intensity in the valleys between the peaks dropped to almost zero (Fig. 5*f*), indicating that the particle was under a spatially coherent illumination.

4.3. Diffraction patterns from a *C. merolae* cell

A series of diffraction patterns were collected from a single *C. merolae* cell, which was in the G/M state before the cell division phase in the cell cycle, under the experimental conditions given in Table 1. Each diffraction pattern was recorded as 12 frames of 5 s exposure (total exposure of 60 s). Fig. 6(*a*) shows a series of diffraction patterns taken at every 1.5°-rotation step around $\varphi = -155°$. The sizes of the speckle peaks (approximately 0.23 μm^{-1}) were consistent with the reciprocal of the size of the cell in the LM image. The diffraction patterns in the off-rotation axis regions gradually changed because the Ewald sphere intersects the 3D diffraction intensity distribution differently. On the other hand, diffraction patterns along the rotation axis were almost independent of rotation.

The diffraction patterns at 12° intervals varied significantly, and then the sizes of the speckle peaks became slightly larger (∼0.40 μm^{-1}) along the horizontal direction at large rotation angles. This variation in speckle size suggested an anisotropic shape of the cell. The C_{sym} values of most of the diffraction patterns were larger than 0.7 (Fig. 6*b*), and the maximum resolution (defined in §3.4) was kept at approximately 27 μm^{-1}, except for in the angular range $-115° < \varphi < -66°$. At these higher tilt angles, background scattering from the edges of the specimen disk frame made the apparent resolution higher. However, the background caused no significant effect on the phase retrieval as shown later (Fig. 6*c*).

Little changes in the diffraction patterns collected at the same rotation angle before and after the data collection suggest little adsorption of molecules to the frozen-hydrated cell, and

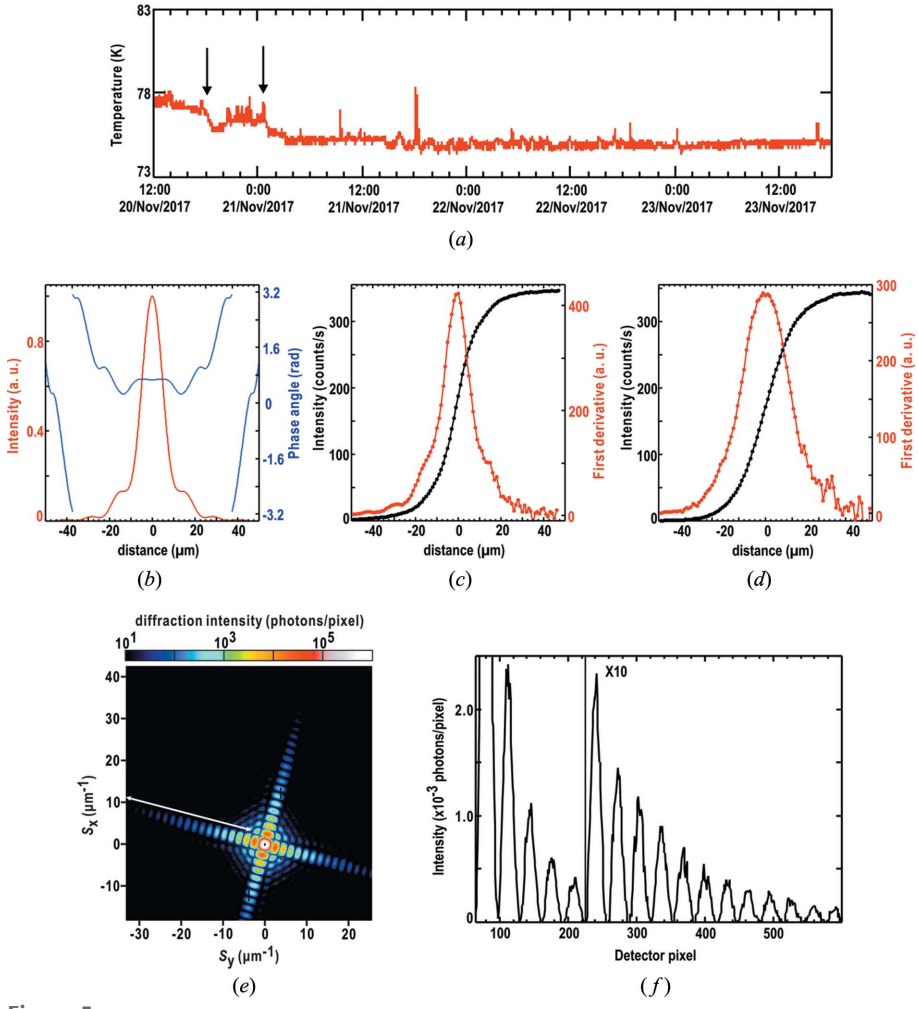

Figure 5
(*a*) Temperature variation of the cryogenic pot during a tomography XDI experiment. The arrows indicate the adjustment of a needle valve attached to the scroll pump. Small spikes appearing in the temperature variation had little influence on the experiment. (*b*) Theoretical curves of the intensity (red line) and phase (blue line) in the diffraction pattern from a pinhole with a diameter of 38 μm expected at the specimen position (Fig. 4*b*). Panels (*c*) and (*d*) show the intensity profiles in the diffraction pattern from a pinhole of 38 μm diameter (red lines and dots) in the vertical and horizontal directions, respectively. The profiles are calculated as the derivative of the intensity variation (black lines and dots) measured by the knife-edge scans. (*e*) Diffraction pattern from a cuboid-shaped cuprous oxide particle with an approximate size of 580 nm recorded after an adjustment of the silicon slits. (*f*) Line profile along one of the flares (white line) in the cross-shaped diffraction pattern.

also little sublimation of water molecules from the cell under the vacuum kept at 5×10^{-5} Pa. In addition, it indicated little radiation damage during the diffraction data collection at the respective temperature. Indeed, the estimated total irradiation dose from the PIN-photodiode measurement (Table 1) was much smaller than the maximum tolerable dose (1.0×10^{10} Gy) for structural analysis at a resolution of 100 nm (Howells *et al.*, 2009).

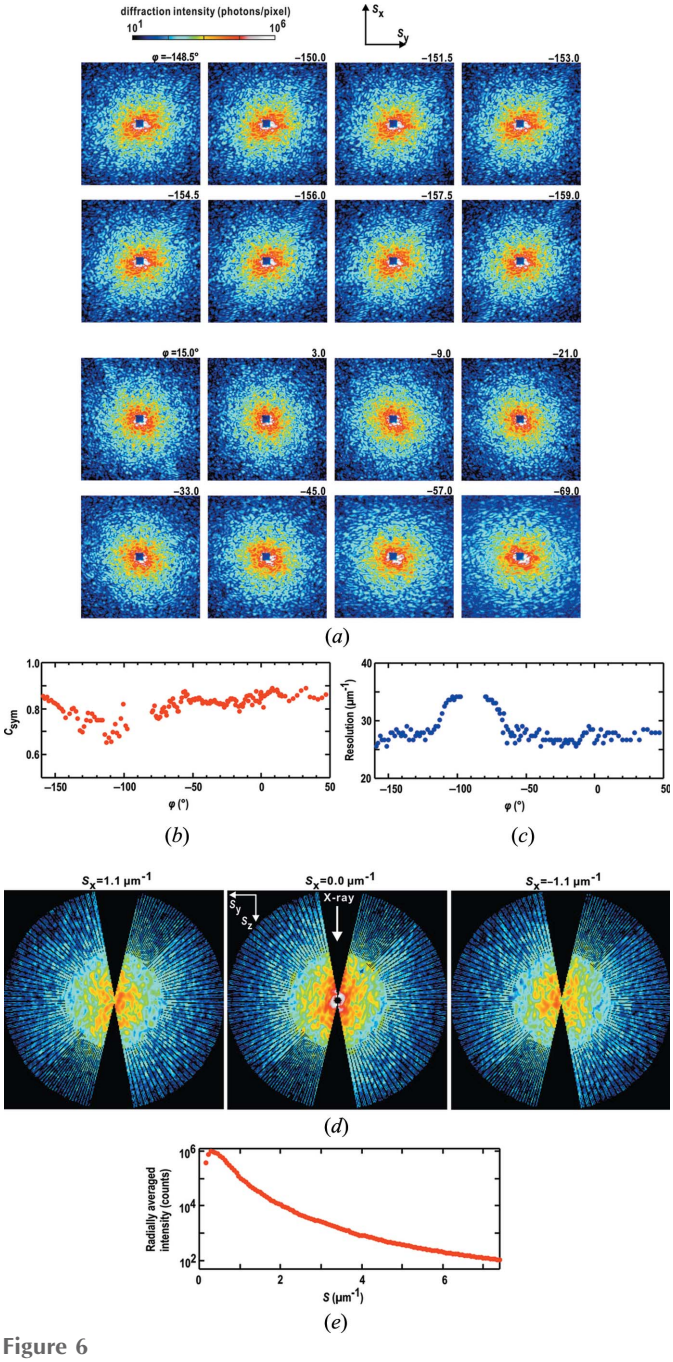

Figure 6
(*a*) Series of diffraction patterns from *C. merolae* during a successive 1.5° rotation around $\varphi = -155°$ (upper panel), and those picked up at an interval of 12.0° (lower panel). The resolution at the edge is 5.62 μm^{-1}, corresponding to 178 nm in real space. Variation of the C_{sym} values (*b*) and maximum resolution (*c*) of the diffraction patterns plotted against the rotation angle. (*d*) Distribution of diffraction intensity in the S_y–S_z planes at S_x = 1.1 (left panel), 0.0 (center) and −1.1 μm^{-1} (right). The resolution at the edge is 14.7 μm^{-1}, corresponding to 68.0 nm in real space. (*e*) The resolution-dependent variation of radially averaged diffraction intensity.

Table 1
Conditions in the diffraction data collection.

Condition	*C. merolae*	*S. cerevisie*
Incident intensity [X-ray photons (20 μm)$^{-2}$ s^{-1}]	3.1×10^9	3.3×10^9
Angular range (°)	–165.0 to −97.5 and −79.5 to +50.0	–79.5 to +81.0
Angular interval (°)	1.5	1.5
Exposure time spent for positional adjustment at each rotation angle (s)	25	25
Exposure time for record a diffraction pattern of the cell / the membrane at each rotation angle (s)	60/60	60/60
Number of diffraction patterns collected	119	107
Total exposure time for the cell including the positional adjustment (s)	10115	9095
Total irradiation dose for the cell including positional adjustment (Gy)	3.92×10^7	3.53×10^7

Fig. 6(*d*) shows three sections in the 3D distribution of the diffraction intensities as viewed along the rotation axis. The distribution of the diffraction intensity likely satisfies the centrosymmetry. In the angular range $-97.5° < \varphi < -79.5°$, diffraction patterns could not be collected because the silicon frame of the specimen disk hindered the incident and diffracted X-rays. The angular range is comparable with or wider than that of standard TEM tomography (Lučić *et al.*, 2005). The radially averaged diffraction intensity displayed a monotonous decrease without any gap in the range from 10^6 to 10^1 photon counts (Fig. 6*e*). This result demonstrated that the diffraction patterns recorded in each 5 s exposure frame were within the dynamic range of the detector.

4.4. Projection and 3D maps of a *C. merolae* cell

The handedness of the PR maps retrieved at a resolution of 136 nm was the same among the most probable maps, although some maps required a π-rotation to achieve optimal overlap with a reference map. Any pair of most probable maps for adjacent rotation angles was similar with respect to the shapes and internal structures (Fig. 7*a*). The T_{ij} value between the best and the second-best PR maps were small for each PR map (Fig. 7*b*), and the crystallographic *R*-factors of the most probable maps were less than 0.2 except for the maps retrieved from diffraction patterns collected in the ranges $-120° < \varphi < -100°$ and $60° < \varphi < 80°$ (Fig. 7*c*).

A 3D map was reconstructed at a resolution of 136 nm by using the back-projection method, and displayed a crystallographic *R*-factor of 0.076. Although a missing wedge was caused by the silicon frame of the specimen disk (Fig. 6*d* and Table 1), it had little influence on the reconstructed 3D map at

the resolution, according to the theory of tomography TEM (Nudelman *et al.*, 2011). The map was composed of a large body with dimensions 5 μm × 5 μm × 4 μm and an accompanied small 1 μm × 1 μm × 1 μm bulge (Fig. 7*d*). The relatively large size of the main body to the small bulge reflects structural characteristics of cells in the G/M phase (Imoto *et al.*, 2011). The electron density distribution inside the cell was non-uniform. The high electron density regions shown in red in Fig. 7(*d*) were thought to be organelles in which nucleic acids and proteins are densely distributed with electron densities of 1.3–1.8 times larger than cytosol (Stuhrmann & Miller, 1978; Cantor & Schimmel, 1980). The structure of the *C. merolae* cell in the G/M phase was investigated using the fluorescence LM images for a chemically labeled specimen (Matsuzaki *et al.*, 2004) and TEM for a thin section of a negatively stained G/M cell (Miyagishima *et al.*, 2001). The 3D map was compared with the images obtained by the two sophisticated methods, by using the fact that XDI gives the distribution of electron densities of the cell without sectioning and chemical labeling.

In the bulge, we identified a high-density region of size 730 nm × 770 nm × 810 nm and interpreted it as an aggregate of nucleic acids and proteins. Taking the mass of a DNA base pair (Dolezel *et al.*, 2003) and the density of DNA (1.7 g cm^{-3}) (Watson *et al.*, 1987), the volume (4.5 × 10^{8} nm^{3}) may be sufficient for the storage of two copies of approximately 1.65 × 10^{7} base pairs of all DNA in *C. merolae* (Nozaki *et al.*, 2007), because the volume of all DNA in a compact packing is estimated to be 1 × 10^{7} nm^{3}. In TEM images of a stained and sectioned specimen, the distribution of nucleic acids was unclear (Miyagishima *et al.*, 2001). In the LM image labeled by fluorescence dyes, DNAs were distributed uniformly (Matsuzaki *et al.*, 2004). To understand the differences regarding the distribution of DNA and proteins among the three techniques, electron density maps at higher resolution are necessary for frozen-hydrated, fluorescence-labeled and stained *C. merolae* cells in the G/M state.

In the main body we found a high-density region located along the envelope. The approximate diameter and circumferential length of the region were 3 μm and 9 μm, respectively. The shape is similar to that of a C-shaped density found in XDI and fluorescence LM studies of chloroplasts isolated from *C. merolae* (Takayama *et al.*, 2015), but the length is longer than those of the isolated ones. The C-shaped density was assigned as an assembly of thylakoid membranes. Therefore, the high-density regions in the main body could also be assignable as assemblies of thylakoid membranes in chloroplast. Chloroplasts of *C. merolae* are known to be duplicated in the G/M phase (Imoto *et al.*, 2011). In future studies, we would trace the numbers, shapes and sizes of the tubular-shaped densities in the cell cycle.

The other map was reconstructed by the 3D PR method applied to the merged 3D distribution of diffraction intensities, with an oversampling ratio of 24.9 up to a resolution of 6.27 μm^{-1} (Fig. 7*e*). The map displayed substantial differences from the back-projection

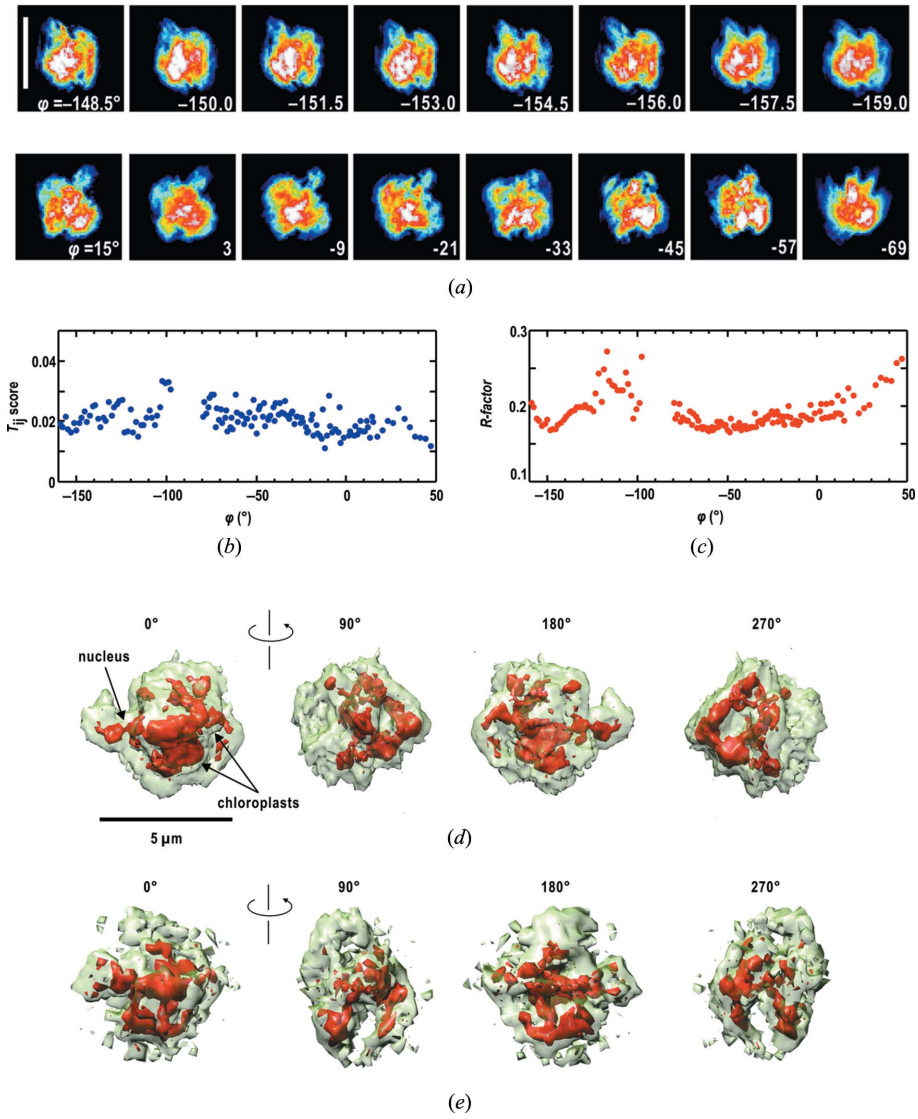

Figure 7
Projection and 3D electron density maps of *C. merolae*. (*a*) Projection electron density maps retrieved from the diffraction patterns in panel (*a*) of Fig. 6 at a resolution of 136 nm. The scale bar is 5 μm. The variation of T_{ij} (*b*) and crystallographic *R*-factor (*c*) values of the most probable PR maps from diffraction patterns are plotted against the rotation angle. Four views of 3D electron density maps of *C. merolae* reconstructed by the back-projection method (*d*) and 3D PR method (*e*). The maps are contoured to demonstrate the cell envelope and high-density regions. The model is illustrated by using the *UCSF Chimera* suite (Pettersen *et al.*, 2004).

map with respect to the size, shape and internal structure. In addition, the crystallographic *R*-factor of 0.139 was approximately twice that of the back-projection map. The surface of the cell was difficult to define from the 3D map due of the presence of noise densities at a significant level distributed outside the region assumed to be the cell envelop. The locations and shapes of the high-density peaks were different from those in the back-projection map and also inconsistent with the projection PR maps (Fig. 7*a*).

4.5. An example of failure in the specimen preparation

Here we report the weak point of the current specimen preparation using SiN membranes in the tomography experiment on a *S. cerevisiae* cell in the G2/M state (before the cell division phase). Fig. 8(*a*) depicts a series of diffraction patterns taken at 12.0°-rotation intervals under the exposure conditions shown in Table 1. Speckle peaks became gradually wide in the equatorial direction (0.45 μm^{-1}) in the angular region $\varphi < -50°$, indicating that the shape of the cell deviated largely from a sphere when viewed near an angle parallel to the incident X-ray beam. Other details are shown in Fig. S1 of the supporting information.

Indeed, the retrieved PR maps have hemi-spherical shapes for $\varphi < -50°$ and a planar surface attached to the membrane (Fig. 8*b*). The 3D map reconstructed by the back-projection method displayed a hemi-spherical shape with a diameter of 4 μm and a thickness of 2.5 μm (Fig. 8*c*), in contrast to spherical shapes in the LM images during the preparation and also in the soft X-ray imaging of yeast cells (Larabell & Le Gros, 2004). The flat facet of the map suggested deformation of the cell structure by the surface tension after the removal of too much buffer solution. A high-density region composed of two triangular-shaped lobes with similar sizes (1.5 μm × 2 μm × 1 μm) was assignable as aggregates of chromosomes after or during duplication. However, it was difficult to deny the possibility that the deformation induced the high-density region.

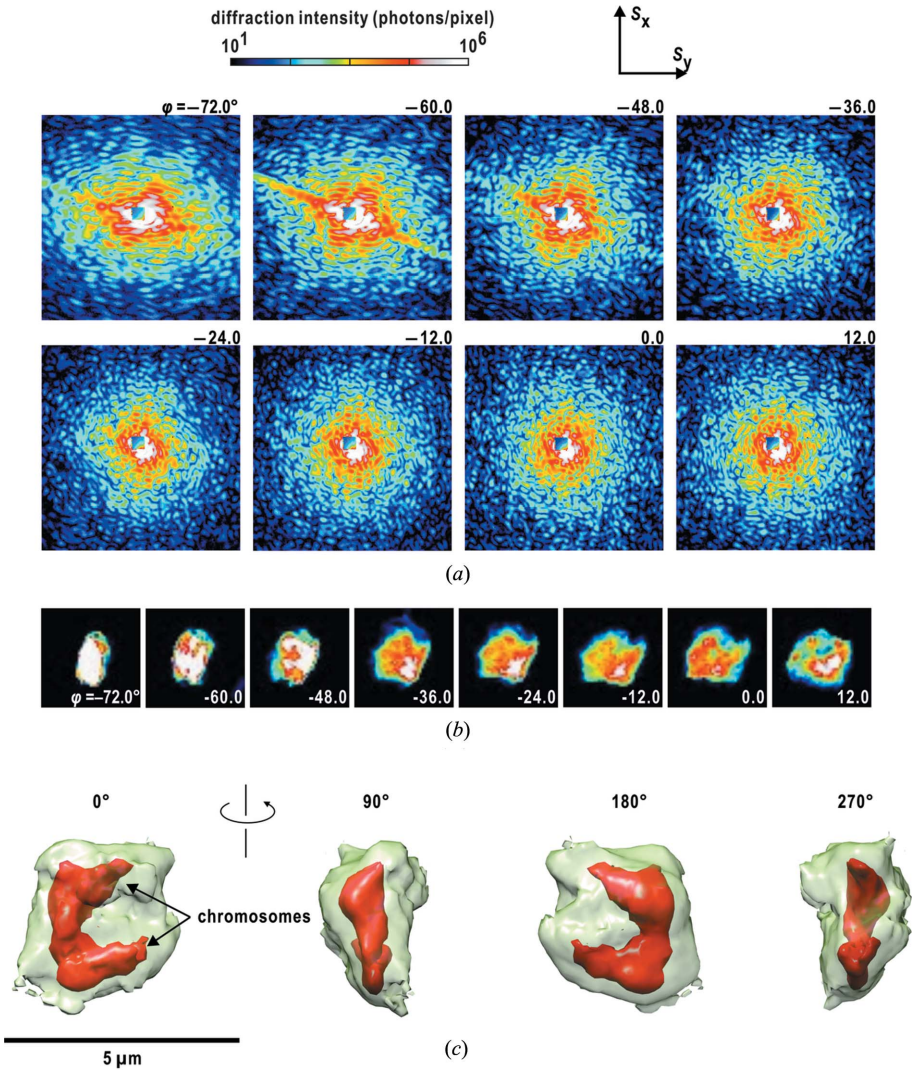

Figure 8
(*a*) Series of diffraction patterns from *S. cerevisiae* picked up at an interval of 12.0°. The resolution at the edge is 6.31 μm^{-1}, corresponding to 158 nm in real space. (*b*) Projection electron density maps of the *S. cereviciae* cell retrieved from the diffraction patterns in panel (*a*) at a resolution of 136 nm. The scale bar is 3 μm. The handedness was the same among the PR maps as in the case of *C. merolae*. However, a π-rotation was necessary for several PR maps. (*c*) Four views of 3D electron density maps of *S. cerevisiae* reconstructed by the back-projection method. The maps are contoured to demonstrate the cell envelope and high-density regions. The model is illustrated by using the *Chimera* suite (Pettersen *et al.*, 2004).

4.6. Estimation for maximum resolution expected under a tolerable irradiation dose

After the tomography experiment for the *C. merolae* cell, a diffraction pattern was accumulated as 552 frames of 5 s exposures in order to study the correlation between irradiation dose and achievable resolution (Fig. 9*a*). In the 2760 s exposure, speckle peaks were recorded at a corner of the detector beyond 20 μm^{-1}, and then the PR map retrieved at a resolution of 33 μm^{-1} (corresponding to a resolution of 30 nm in real space) provided detailed projection structures of the cell.

The accumulation of diffraction patterns demonstrated that the longer exposure yielded diffraction patterns with better signal-to-noise ratio at higher resolution (Fig. 9*b*). The maximum resolution displayed a linear correlation with the logarithm of the exposure time (Fig. 9*c*). In addition, equation (1) gives the

number of diffraction patterns necessary in 3D reconstruction at a desired resolution (Fig. 9*d*). From the correlation and the number of exposures, we estimated the maximum achievable resolution in a tomography XDI experiment for the *C. merolae* cell in the G/M state under the conditions shown in Table 1. By referring to the maximum tolerable irradiation dose at a desired resolution proposed in the literature (Howells *et al.*, 2009), the maximum achievable resolution of the *C. merolae* cell in the G/M state was estimated to be approximately 20 nm (Fig. 9*e*), at which resolution supramolecular complexes and large protein molecules would be approximated as voxels composing the 3D density map.

The total irradiance was estimated without the 25 s exposure necessary for the positional adjustment at each rotation angle. However, the exposure time necessary to collect a diffraction pattern up to a resolution of approximately 50 μm^{-1} was estimated to be 3000 s. Therefore, the total irradiation dose necessary for the positional adjustment has only a small contribution in the estimation of the achievable resolution.

5. Discussion

The cryogenic pot dedicated to tomography XDI experiments (Figs. 2 and 5*a*) was used in the collection of diffraction patterns from a frozen-hydrated single bacterial cell (Fig. 6) to visualize the whole 3D electron density at a resolution of 136 nm (Fig. 7). Here we discuss the future improvements and prospects of tomography XDI experiments by using the developed diffraction apparatus.

5.1. Performance of the diffraction apparatus

One of the current problems is the time spent on the positional adjustment of the specimen after each rotation. Through tomography XDI experiments we found a reproducible correlation between the positional shifts of the specimen and the rotation angle of the goniometer. Therefore, more rapid and automatic adjustment will be possible

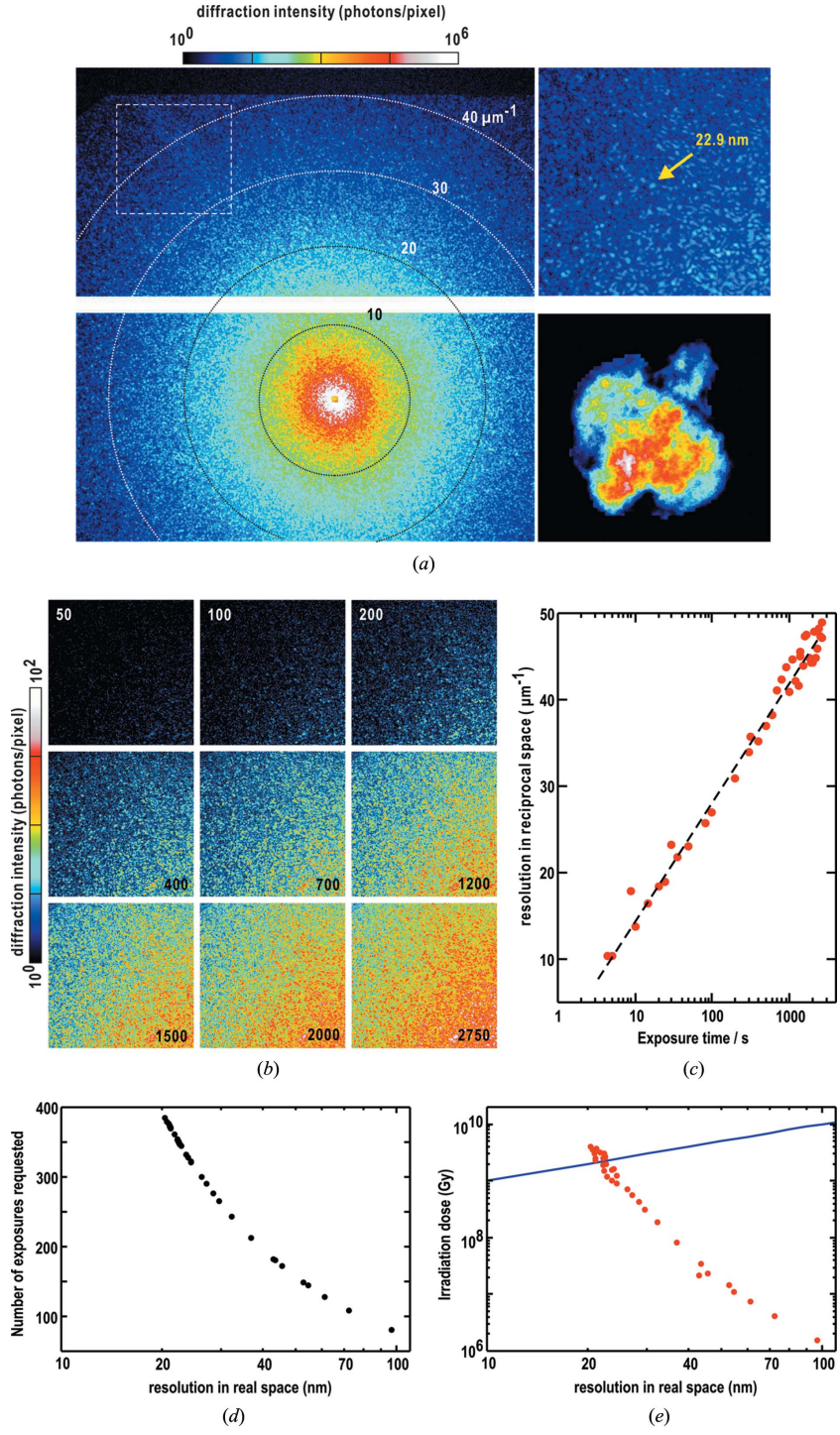

Figure 9
(*a*) The left panel shows a diffraction pattern of a *C. merolae* cell in the G/M phase recorded at an exposure time of 2760 s. The dotted circles display the resolution in reciprocal space. The area indicated by the dashed box is magnified in the upper-right panel. The lower-right panel is a projection electron density map retrieved from the diffraction pattern in the left panel at a resolution of 34.1 nm. (*b*) Representative diffraction patterns at an edge region of the detector during the accumulation of 552 frames of 5 s exposure. (*c*) The variation of the maximum resolution of diffraction pattern plotted against the exposure time. The dashed line indicates a linear correlation between the maximum resolution in reciprocal space and the logarithm of the exposure time. (*d*) Plot showing the number of exposures to achieve a spatial resolution in real space. (*e*) Estimated radiation dose in a tomography experiment to collect diffraction patterns necessary for the 3D reconstruction of a map at a desired resolution in real space (red circles). The blue line is the resolution-dependence of the maximum tolerable radiation dose reported in the literature (Howells *et al.*, 2009).

by incorporating the empirically obtained correlation as a database in the control software in near future experiments. In addition, through the recent experiences on semi-automatic data collection and careful operation, the control program could be executed in full-automatic mode in the near future.

To improve the performance of tomography XDI experiments, the beam position would ideally be kept at its initial position to ensure spatially coherent illumination. Because it took at least two hours for fine-tuning of the optical elements, such as the pinhole, slits and beamstop (Fig. 4*a*), it is necessary to reduce the time spent on tuning the beam position. Although the first silicon crystal of the double-crystal monochromator is cooled by liquid nitrogen, it suffers from the heat load caused by the undulator radiation not being used in the experiments. Then, an unexpected small deformation in the surface structure of the first monochromator causes a decrease of intensity, a slight change in the beam position at the specimen and parasite scattering from the optics. To reduce non-necessary undulator radiation, narrowing of the front-end slits is one way of suppressing the non-linear behavior due to positional changes of the X-ray beam. In addition, because the heat load of the monochromator also correlates with the number of X-ray pulses in a unit period of time, *i.e.* the bunch structures in the synchrotron ring, the selection of an operation mode may also be a factor in the stable supply of monochromatic X-ray beams.

5.2. Specimen preparation

SiN membranes are conventionally used in XDI experiments of biological specimens (Nishino *et al.*, 2009; Jiang *et al.*, 2010; Song *et al.*, 2014; Takayama *et al.*, 2015; Oroguchi *et al.*, 2015; Kobayashi *et al.*, 2016*a*). Here, we present two examples of the 3D reconstruction of bacterial cells at a resolution of 136 nm. While the 3D density map of the *C. merolae* cell was globular (Fig. 7*d*), the *S. cereviciae* cell had a hemi-spherical shape with a flat facet (Fig. 8*c*). This suggests the possibility that excessive removal of buffer solution causes the deformation of cells due to the surface tension of the buffer solution. Therefore, we should be careful in the removal of buffer solution, or the present specimen preparation technique should be improved or changed.

One of the possible improvements to avoid this deformation of cell structures is the utilization of the free-standing technique by using a thin membrane with a small hole in the center. A single cell could be suspended in a droplet of buffer solution adsorbed in the hole. Another improvement is the utilization of a microcapillary, in which a buffer solution containing a single cell is aspirated, as reported in X-ray imaging experiments performed at the Swiss Light Source (Diaz *et al.*, 2015). Then, a single cell floats in the buffer solution and is free from contact with the edge of the hole or the inner surface of the capillary.

In utilizing both techniques, we should pay attention to the total reflection of part of the X-ray beam occurring at grazing incidence on the surface of the droplet or that of the capillary tube. The incident X-ray beam produced by a pinhole has a tail with a significant intensity level of the order of 10^7 X-ray photons μm^{-2} s^{-1} (Figs. 5*c* and 5*d*). Then, a total reflection, which would appear as a strong streak in the small-angle region, overlaps with the diffraction patterns from a specimen particle. Therefore, we must study both the methods and the PR calculation for diffraction patterns without the streak region, to visualize the structures of fragile biological cells.

5.3. Data processing

Here we discuss future improvements in data processing and structural analysis. Although the present study defines a position as a pixel (or voxel) with finite size, it is best to treat the beam center position as a point to reduce uncertainties in the PR calculations. A diffraction pattern from a cuprous oxide particle with dimensions of more than 1 μm (Fig. 5*e*) can be utilized to better estimate the beam center position, because of the short interval and strong intensities of the interference pattern. Then, sub-pixel shifts of the detector position (Chushkin & Zontone, 2013) can be used as a strategy to obtain a more precise determination of the position. In this regard, the intensity distribution is also treated as a function of the scattering vector rather than the pixel/voxel position. These would improve the centrosymmetry (Fig. 6*b*) in the 2D and 3D distribution of the diffraction intensity.

5.4. 3D reconstruction

In this study we used two different algorithms for reconstructing 3D maps from tomography diffraction patterns. The 3D maps reconstructed by using the back-projection method display smaller crystallographic *R*-factors than those reconstructed using the 3D PR method, and substantial differences from the maps using the 3D PR method (Figs. 7, 8 and Fig. S1 of the supporting information). On the 3D maps reconstructed using the back-projection method it is easier to identify cell surfaces and to interpret the internal structures than those reconstructed from the 3D PR calculation. It is therefore worth discussing the pros and cons of the two methods.

In the back-projection method, maps from failed PR calculations can be easily excluded by assessing the similarity between PR maps at adjacent angles (Sekiguchi *et al.*, 2017). The handedness and π-rotation of PR maps must be manually assessed. In addition, the normalization of the PR maps is easy, because a specimen cell is completely irradiated in the coherent region of the incident X-ray beam at every rotation angle by the positional adjustment for every rotation.

The 3D PR method yields a 3D map through a single calculation. For the calculation, diffraction patterns must be rigorously normalized with respect to the intensity of the incident X-ray beam. In addition, diffraction patterns should be collected at fine angular steps to satisfy an oversampling ratio required in the 3D PR calculation. The simultaneous use of 3D PR and equally sloped tomography with oversampling reconstruction (EST) (Miao *et al.*, 2005*b*) is a possible way to address the success and failure of the 3D PR calculation, although the diffraction data collection must be performed to satisfy the condition required for the EST method.

In both methods the handedness of the 3D maps is still difficult to determine experimentally because biological cells contain an insufficient amount of anomalous scatterers to be used for the determination in the X-ray wavelength range used. In the single-particle analysis of TEM, the handedness is determined by images of a specimen recorded in two different orientations with respect to the direction of the incident electron beam (Elmlund & Elmlund, 2015). In XDI, LM images of cells mounted on a goniometer may help to address the handedness.

5.5. Structure refinement

In this study, although the structural analyses were temporarily performed at a resolution of 136 nm, the resolution will be extended in future experiments. In fact, for a single biological cell of size 5 µm, the achievable resolution of a 3D reconstruction is estimated to be approximately 20 nm under the maximum tolerable irradiation dose (Fig. 9*e*). For unambiguously addressing the fine structures, structure refinement of the reconstructed 3D maps will be necessary, just as in the case of crystal structural analysis. For instance, structure refinement of protein molecules simultaneously minimizes the crystallographic *R*-factor in reciprocal space and the internal energy and/or deviation from the ideal stereochemistry in real space (Zhang & Main, 1990). However, because the constraints on the electron density distribution in real space are still unknown for biological cells at present, it is necessary to develop real-space constraints for structural analyses at a resolution of 20 nm.

5.6. Structural variation among many individual cells

Owing to structural variation among individual cells depending on cell cycle, nutritional state and light condition, we must be careful when we discuss biological meaning in referring to the structure of an individual cell visualized by the XDI tomography method. We are planning to verify the condition of the targeted cell by flow cytometry or pick up the cell of a targeted condition by a cell sorter before specimen preparation. In addition, we have another XDI technique for collecting several tens of thousands of diffraction patterns from individual cells in five days by using the X-ray free-electron laser at SACLA (Takayama *et al.*, 2015; Oroguchi *et al.*, 2015; Kobayashi *et al.*, 2016*a*,*b*). The diffraction patterns provide projection electron density maps of individual cells. Then, by comparing the 3D maps from tomography XDI and the projection maps from XDI using X-ray free-electron laser pulses, we expect to obtain multi-aspect structural information, which is meaningful for both molecular biology and cell biology.

6. Conclusion

Through the development of a cryogenic pot, miscellaneous devices, specimen preparation techniques and experimental procedures including software and tomography XDI experiments were successfully performed. The present study also suggests the possible resolution limit for structural analysis of biological cells under a maximum tolerable irradiation dose. In the near future, reconstructed 3D maps of whole cells will illustrate the electron density distribution inside a cell at a resolution of 20 nm, and contribute to provide new insight into the nature of intracellular structures in combination with images from fluorescence LM on the distribution of molecules, TEM of sectioned specimens and other imaging techniques.

Acknowledgements

We thank Professor Sachihiro Matsunaga of Tokyo University of Science for his kind supply of *C. merolae*. The XDI diffraction data for structural analyses were collected at BL29XUL of SPring-8 (proposal Nos. 20090097, 20100035, 20110006, 20140096, 20150098, 20160084, 20170013). We used BL24XU of SPring-8 in the development of the slit otics (proposal No. 2016B3201).

Funding information

This study was supported by a grant for XFEL key technology, and by the X-ray Free Electron Laser Priority Strategy Program from the Ministry of Education, Culture, Sports, Science and Technology (MEXT) to MN and MY. In addition, specimen preparation and software development were supported by grants from the Japan Society for the Promotion of Science to MN (jp17654084, jp23120525, jp24654140, jp25120725, jp16H02218), to YS (No. jp15J01707) and to AK (No. jp15J01831), and grants from the MEXT to MN (Nos. jp15076210, jp20050030).

References

Adrian, M., Dubochet, J., Lepault, J. & McDowall, A. W. (1984). *Nature (London)*, **308**, 32–36.
Al-Amoudi, A., Chang, J., Leforestier, A., McDowall, A., Salamin, L., Norlén, L., Richter, K., Blanc, N., Studer, D. & Dubochet, J. (2004). *EMBO J.* **23**, 3583–3588.
Appen, A. von & Beck, M. (2016). *J. Mol. Biol.* **428**, 2001–2010.
Baker, L. A. & Rubinstein, J. L. (2010). *Methods Enzymol.* **481**, 371–388.
Born, M. & Wolf, E. (1999). *Principles of Optics*, 7th (expanded) ed. Cambridge University Press.
Boutet, S. & Robinson, I. K. (2006). *J. Synchrotron Rad.* **13**, 1–7.
Cantor, C. R. & Schimmel, P. R. (1980). *Biophysical Chemistry*, Part II, *Techniques for the Study of Biological Structure and Function.* New York: W. H. Freeman and Company.
Chushkin, Y. & Zontone, F. (2013). *J. Appl. Cryst.* **46**, 319–323.
DeLong, L. E., Symko, O. G. & Wheatley, J. C. (1971). *Rev. Sci. Instrum.* **42**, 147–150.
Diaz, A., Malkova, B., Holler, M., Guizar-Sicairos, M., Lima, E., Panneels, V., Pigino, G., Bittermann, A. G., Wettstein, L., Tomizaki, T., Bunk, O., Schertler, G., Ishikawa, T., Wepf, R. & Menzel, A. (2015). *J. Struct. Biol.* **192**, 461–469.
Dolezel, J., Bartos, J., Voglmayr, H. & Greilhuber, J. (2003). *Cytometry*, **51A**, 127–128.
Dubochet, J., Adrian, M., Chang, J.-J., Homo, J.-C., Lepault, J., McDowall, A. & Schultz, P. (1988). *Q. Rev. Biophys.* **21**, 129–228.
Dubochet, J., Lepault, J., Freeman, R., Berriman, J. A. & Homo, J.-C. (1982). *J. Microsc.* **128**, 219–237.
Dubochet, J. & McDowall, A. W. (1981). *J. Microsc.* **124**, 3–4.
Elmlund, D. & Elmlund, H. (2015). *Annu. Rev. Biochem.* **84**, 499–517.

Fienup, J. R. (1982). *Appl. Opt.* **21**, 2758–2769.
Frank, J. (2006). *Three-Dimensional Electron Microscopy of Macromolecular Assemblies.* Oxford University Press.
Gibson, L. F. & Khoury, J. T. (1986). *Lett. Appl. Microbiol.* **3**, 127–129.
Grassucci, R. A., Taylor, D. J. & Frank, J. (2007). *Nat. Protoc.* **2**, 3239–3246.
Hell, S. W. & Wichmann, J. (1994). *Opt. Exp.* **19**, 780–782.
Herman, G. T. (2009). *Fundamentals of Computerized Tomography.* London: Springer.
Howells, M. R., Beetz, T., Chapman, H. N., Cui, C., Holton, J. M., Jacobsen, C. J., Kirz, J., Lima, E., Marchesini, S., Miao, H., Sayre, D., Shapiro, D. A., Spence, J. C. E. & Starodub, D. (2009). *J. Electron Spectrosc. Relat. Phenom.* **170**, 4–12.
Hsieh, C.-E., Leith, A., Mannella, C. A., Frank, J. & Marko, M. (2006). *J. Struct. Biol.* **153**, 1–13.
Huang, B., Bates, M. & Zhuang, X. (2009). *Annu. Rev. Biochem.* **78**, 993–1016.
Imoto, Y., Yoshida, Y., Yagisawa, F., Kuroiwa, H. & Kuroiwa, T. (2011). *J. Electron Microsc. (Tokyo)*, **60**, S117–S136.
Jaffe, E., Nachman, R., Becker, C. & Minick, R. (1973). *J. Clin. Invest.* **52**, 2745–2756.
Jiang, H., Song, C., Chen, C. C., Xu, R., Raines, K. S., Fahimian, B. P., Lu, C. H., Lee, T. K., Nakashima, A., Urano, J., Ishikawa, T., Tamanoi, F. & Miao, J. (2010). *Proc. Natl Acad. Sci. USA*, **107**, 11234–11239.
Kirz, J., Jacobsen, C. & Howells, M. (1995). *Q. Rev. Biophys.* **28**, 33–130.
Kobayashi, A., Sekiguchi, Y., Oroguchi, T., Okajima, K., Fukuda, A., Oide, M., Yamamoto, M. & Nakasako, M. (2016*a*). *J. Synchrotron Rad.* **23**, 975–989.
Kobayashi, A., Sekiguchi, Y., Takayama, Y., Oroguchi, T., Shirahama, K., Torizuka, Y., Manoda, M., Nakasako, M. & Yamamoto, M. (2016*b*). *Rev. Sci. Instrum.* **87**, 053109.
Kodama, W. & Nakasako, M. (2011). *Phys. Rev. E*, **84**, 021902.
Kuo, C. H., Chen, C. H. & Huang, M. H. (2007). *Adv. Funct. Mater.* **17**, 3773–3780.
Larabell, C. A. & Le Gros, M. A. (2004). *Mol. Biol. Cell*, **15**, 957–962.
Lučić, V., Förster, F. & Baumeister, W. (2005). *Annu. Rev. Biochem.* **74**, 833–865.
Marchesini, S., He, H., Chapman, H. N., Hau-Riege, S. P., Noy, A., Howells, M. R., Weierstall, U. & Spence, J. C. H. (2003). *Phys. Rev. B*, **68**, 140101.
Maser, J., Osanna, A., Wang, Y., Jacobsen, C., Kirz, J., Spector, S., Winn, B. & Tennant, D. (2000). *J. Microsc.* **197**, 68–79.
Matsuzaki, M., Misumi, O., Shin-I, T., Maruyama, S., Takahara, M., Miyagishima, S., Mori, T., Nishida, K., Yagisawa, F., Nishida, K., Yoshida, Y., Nishimura, Y., Nakao, S., Kobayashi, T., Momoyama, Y., Higashiyama, T., Minoda, A., Sano, M., Nomoto, H., Oishi, K., Hayashi, H., Ohta, F., Nishizaka, S., Haga, S., Miura, S., Morishita, T., Kabeya, Y., Terasawa, K., Suzuki, Y., Ishii, Y., Asakawa, S., Takano, H., Ohta, N., Kuroiwa, H., Tanaka, K., Shimizu, N., Sugano, S., Sato, N., Nozaki, H., Ogasawara, N., Kohara, Y. & Kuroiwa, T. (2004). *Nature (London)*, **428**, 653–657.
Meents, A., Gutmann, S., Wagner, A. & Schulze-Briese, C. (2010). *Proc. Natl Acad. Sci. USA*, **107**, 1094–1099.
Messaoudii, C., Boudier, T., Sanchez Sorzano, C. O. & Marco, S. (2007). *BMC Bioinformatics*, **8**, 288.
Miao, J., Charalambous, P., Kirz, J. & Sayre, D. (1999). *Nature (London)*, **400**, 342–344.
Miao, J., Förster, F. & Levi, O. (2005*b*). *Phys. Rev. B*, **72**, 052103.
Miao, J., Ishikawa, T., Johnson, B., Anderson, E. H., Lai, B. & Hodgson, K. O. (2002). *Phys. Rev. Lett.* **89**, 088303.
Miao, J., Ishikawa, T., Robinson, I. K. & Murnane, M. M. (2015). *Science*, **348**, 530–535.
Miao, J., Nishino, Y., Kohmura, Y., Johnson, B., Song, C., Risbud, S. H. & Ishikawa, T. (2005*a*). *Phys. Rev. Lett.* **95**, 085503.
Miyagishima, S., Kuroiwa, H. & Kuroiwa, T. (2001). *Planta*, **212**, 517–528.
Nakasako, M. (2018). *X-ray Diffraction Imaging of Biological Cells*, Vol. 210 of *Springer Series in Optical Sciences.*, Tokyo: Springer Nature.
Nakasako, M., Takayama, Y., Oroguchi, T., Sekiguchi, Y., Kobayashi, A., Shirahama, K., Yamamoto, M., Hikima, T., Yonekura, K., Maki-Yonekura, S., Kohmura, Y., Inubushi, Y., Takahashi, Y., Suzuki, A., Matsunaga, S., Inui, Y., Tono, K., Kameshima, T., Joti, Y. & Hoshi, T. (2013). *Rev. Sci. Instrum.* **84**, 093705.
Nishino, Y., Takahashi, Y., Imamoto, N., Ishikawa, T. & Maeshima, K. (2009). *Phys. Rev. Lett.* **102**, 018101.
Nozaki, H., Takano, H., Misumi, O., Terasawa, K., Matsuzaki, M., Maruyama, S., Nishida, K., Yagisawa, F., Yoshida, Y., Fujiwara, T., Takio, S., Tamura, K., Chung, S., Nakamura, S., Kuroiwa, H., Tanaka, K., Sato, N. & Kuroiwa, T. (2007). *BMC Biol.* **5**, 1–8.
Nudelman, F., de With, G. S. & Sommerdijk, N. A. J. M. (2011). *Soft Matter*, **7**, 17–24.
Oikonomou, C. M., Chang, Y.-W. & Jensen, G. J. (2016). *Nat. Rev. Microbiol.* **14**, 205–220.
Oroguchi, T. & Nakasako, M. (2013). *Phys. Rev. E*, **87**, 022712.
Oroguchi, T., Sekiguchi, Y., Kobayashi, A., Masaki, Y., Fukuda, A., Hashimoto, S., Nakasako, M., Ichikawa, Y., Kurumizaka, H., Shimizu, M., Inui, Y., Matsunaga, S., Kato, T., Namba, K., Yamaguchi, K., Kuwata, K., Kameda, H., Fukui, N., Kawata, Y., Kameshima, T., Takayama, Y., Yonekura, K. & Yamamoto, M. (2015). *J. Phys. B At. Mol. Opt. Phys.* **48**, 184003.
Oroguchi, T., Yoshidome, T., Yamamoto, T. & Nakasako, M. (2018). *Nano Lett.* **18**, 5192–5197.
Pettersen, E. F., Goddard, T. D., Huang, C. C., Couch, G. S., Greenblatt, D. M., Meng, E. C. & Ferrin, T. E. (2004). *J. Comput. Chem.* **25**, 1605–1612.
Radermacher, M. (1988). *J. Electron Microsc. Tech.* **9**, 359–394.
Robards, A. W. & Sleytr, U. B. (1985). *Low Temperature Methods in Biological Electron Microscopy.* Amsterdam: Elsevier.
Rodriguez, J. A., Xu, R., Chen, C.-C., Huang, Z., Jiang, H., Chen, A. L., Raines, K. S., Pryor Jr, A., Nam, D., Wiegart, L., Song, C., Madsen, A., Chushkin, Y., Zontone, F., Bradley, P. J. & Miao, J. (2015). *IUCrJ*, **2**, 575–583.
Rodriguez, J. A., Xu, R., Chen, C.-C., Zou, Y. & Miao, J. (2013). *J. Appl. Cryst.* **46**, 312–318.
Schneider, G., Guttmann, P., Heim, S., Rehbein, S., Mueller, F., Nagashima, K., Heymann, J. B., Müller, W. G. & McNally, J. G. (2010). *Nat. Methods*, **7**, 985–987.
Sekiguchi, Y., Hashimoto, S., Kobayashi, A., Oroguchi, T. & Nakasako, M. (2017). *J. Synchrotron Rad.* **24**, 1024–1038.
Sekiguchi, Y., Oroguchi, T. & Nakasako, M. (2016). *J. Synchrotron Rad.* **23**, 312–323.
Sekiguchi, Y., Oroguchi, T., Takayama, Y. & Nakasako, M. (2014*b*). *J. Synchrotron Rad.* **21**, 600–612.
Sekiguchi, Y., Yamamoto, M., Oroguchi, T., Takayama, Y., Suzuki, S. & Nakasako, M. (2014*a*). *J. Synchrotron Rad.* **21**, 1378–1383.
Shapiro, D., Thibault, P., Beetz, T., Elser, V., Howells, M., Jacobsen, C., Kirz, J., Lima, E., Miao, H., Neiman, A. M. & Sayre, D. (2005). *Proc. Natl Acad. Sci.* **102**, 15343–15346.
Song, C., Takagi, M., Park, J., Xu, R., Gallagher-Jones, M., Imamoto, N. & Ishikawa, T. (2014). *Biophys. J.* **107**, 1074–1081.
Stuhrmann, H. B. & Miller, A. (1978). *J. Appl. Cryst.* **11**, 325–345.
Takayama, Y., Inui, Y., Sekiguchi, Y., Kobayashi, A., Oroguchi, T., Yamamoto, M., Matsunaga, S. & Nakasako, M. (2015). *Plant Cell Physiol.* **56**, 1272–1286.
Takayama, Y. & Nakasako, M. (2012). *Rev. Sci. Instrum.* **83**, 054301.
Tamasaku, K., Tanaka, Y., Yabashi, M., Yamazaki, H., Kawamura, N., Suzuki, M. & Ishikawa, T. (2001). *Nucl. Instrum. Methods Phys. Res. A*, **467–468**, 686–689.
Watson, J. P., Hopkins, N. H., Roberts, J. W., Steitz, J. A. & Weiner, A. M. (1987). *Molecular Biology of the Gene*, 4th ed. Menlo Park: Benjamin Cummings.
Zhang, K. Y. J. & Main, P. (1990). *Acta Cryst.* A**46**, 41–46.
Zhao, X., Norris, S. & Liu, J. (2014). *Biochemistry*, **53**, 4323–4333.